

Calibrated Hyperspectral Image Reconstruction via Graph-based Self-Tuning Network

Jiamian Wang¹, Yulun Zhang², Xin Yuan³, Ziyi Meng⁴, and Zhiqiang Tao¹

¹Santa Clara University, ²ETH Zürich, ³Westlake University, ⁴Kuaishou Technology

JWang16@scu.edu; yulun100@gmail.com; xyuan@westlake.edu.cn;
mengziyi64@163.com; ztao@scu.edu.

Abstract

Recently, hyperspectral imaging (HSI) has attracted increasing research attention, especially for the ones based on a coded aperture snapshot spectral imaging (CASSI) system. Existing deep HSI reconstruction models are generally trained on paired data to retrieve original signals upon 2D compressed measurements given by a particular optical hardware mask in CASSI, during which the mask largely impacts the reconstruction performance and could work as a “model hyperparameter” governing on data augmentations. This mask-specific training style will lead to a hardware miscalibration issue, which sets up barriers to deploying deep HSI models among different hardware and noisy environments. To address this challenge, we introduce mask uncertainty for HSI with a complete variational Bayesian learning treatment and explicitly model it through a mask decomposition inspired by real hardware. Specifically, we propose a novel Graph-based Self-Tuning (GST) network to reason uncertainties adapting to varying spatial structures of masks among different hardware. Moreover, we develop a bilevel optimization framework to balance HSI reconstruction and uncertainty estimation, accounting for the hyperparameter property of masks. Extensive experimental results and model discussions validate the effectiveness (over 33/30 dB) of the proposed GST method under two miscalibration scenarios and demonstrate a highly competitive performance compared with the state-of-the-art well-calibrated methods. Our code and pre-trained model are available at https://github.com/Jiamian-Wang/mask_uncertainty_spectral_SCI

1. Introduction

Hyperspectral imaging (HSI) provides richer signals than the traditional RGB vision and has broad applications across agriculture [10, 23, 25], medical imaging [14, 24], remote sensing [3, 45], etc. Various HSI systems have been

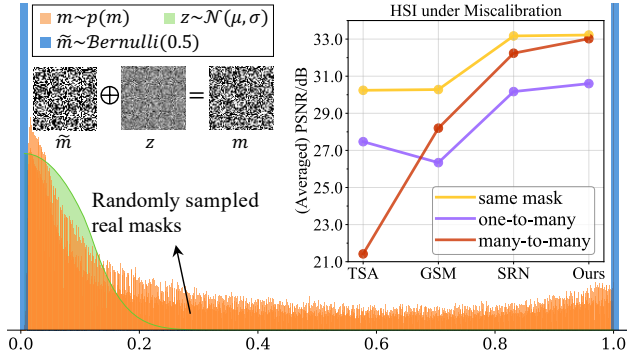


Figure 1. Illustration of real mask decomposition and HSI performance under miscalibration. *Upper left:* A real mask $m \sim p(m)$ can be decomposed into an unknown clean mask \tilde{m} plus random noise z . The mask distribution (histogram) is plotted by realistic hardware mask values. *Upper right:* Performance comparison under three different settings, including 1) the **same mask** for training/testing, 2) training on one mask and testing on multiple masks (**one-to-many**), and 3) training with random masks and testing on a held-out mask set (**many-to-many**).

built and studied in recent years, among which, the coded aperture snapshot spectral imaging (CASSI) system [8, 42] stands out due to its passive modulation property and has attracted increasing research attentions [13, 22, 28, 30, 38, 44] in the computer vision community. The CASSI system adopts a hardware encoding & software decoding schema. It first utilizes an optical hardware mask to compress hyperspectral signals into a 2D measurement and then develops software algorithms to retrieve original signals upon the coded measurement conditioning on one particular mask used in the system. Therefore, the hardware mask generally plays a key role in reconstructing hyperspectral images and may exhibit a strongly-coupled (*one-to-one*) relationship with its reconstruction model.

While deep HSI networks [13, 28, 36] have recently shown a promising performance on high-fidelity reconstruction and real-time inference, they mainly treat the hardware mask as a fixed “model hyperparameter” (governing data augmentations on the compressed measurements) and

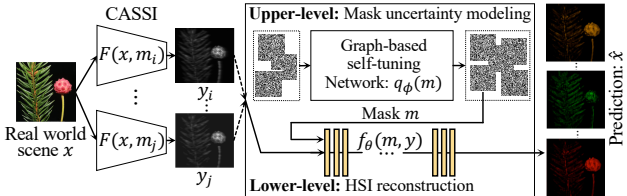


Figure 2. Illustration of the proposed method. Under the framework of bilevel optimization, a Graph-based Self-Tuning (GST) network models mask uncertainty by approximating mask distribution. A reconstruction network $f_\theta(m, y)$ produces retrieved HSI \hat{x} by taking mask as hyperparameter. Our model could be applied in multiple CASSI systems with different masks.

train the reconstruction network on the paired hyperspectral images and measurements given the same mask. Empirically, this will cause a **hardware miscalibration** issue – the mask used in the pre-trained model is unpaired with the real captured measurement – when deploying a single deep reconstruction network among multiple hardware systems (usually with different masks, or different responses even using the same mask due to fabrication errors). As shown in Fig. 1, the performance of deep reconstruction networks pre-trained with one specific mask will badly degrade when applying in different unseen masks (*one-to-many*). Rather than re-training models on each new mask, which is inflexible for practical usage, we are more interested in training a single model that could **adapt to different hardware** by exploring and exploiting **uncertainties** among masks.

One possible solution is to train a deep network over multiple CASSI systems, *i.e.*, using multiple masks and their corresponding encoded measurements following the deep ensemble [19] strategy. However, due to the distinct spatial patterns of each mask and its hyperparameter property, directly training the network with randomly sampled masks still cannot achieve a well-calibrated performance and sometimes performs even worse, *e.g.*, *many-to-many* of TSA-Net [28] in Fig. 1. Hence, we delve into one possible mask decomposition observed from the real hardware (see Fig. 1), which treats a mask as the unknown clean one plus random noise like Gaussian. We consider the noise stemming from two practical sources: 1) the hardware fabrication in real CASSI systems and 2) the functional mask values caused by different lighting environments. Notably, rather than modeling the entire mask distribution, which is challenging due to the high-dimensionality of a 2D map, we explicitly model the mask uncertainty as Gaussian noise centering around a given mask through its decomposition and resort to learn *self-tuning variances* adapting to mask structures among different hardware.

In this study, we propose a novel Graph-based Self-Tuning (GST) network to model mask uncertainty upon variational Bayesian learning and hyperparameter optimization techniques. On the one hand, we approximate the mask posterior distribution with variational inference under the

given prior from real mask values, leading to a smoother mask distribution with smaller variance supported by empirical evidence. On the other hand, we leverage graph convolution neural networks to instantiate a stochastic encoder to reason uncertainties varying to different spatial structures of masks. Moreover, we develop a bilevel optimization framework to balance the HSI reconstruction performance and the mask uncertainty estimation, accounting for the high sensitive network responses to the mask changes. We summarize the contributions of this work as follows.

- We introduce *mask uncertainty* for CASSI to calibrate a single deep reconstruction network applying in multiple hardware, which brings a promising research direction to improve the robustness and flexibility of deploying CASSI systems to retrieve hyperspectral signals in real-world applications. To our best knowledge, this is the first work to explicitly explore and model mask uncertainty in the HSI reconstruction problem.
- A complete variational Bayesian learning framework has been provided to approximate the mask distribution based on a mask decomposition induced by real hardware. Moreover, we design and develop a bilevel optimization framework to jointly achieve high-fidelity HSI reconstruction and mask uncertainty estimation.
- We propose a novel Graph-based Self-Tuning (GST) network to automatically capture uncertainties varying to different spatial structures of 2D masks, leading to a smoother mask distribution over real samples and working as an effective data augmentation method.
- Extensive experimental results on both simulation data and real data demonstrate the effectiveness (over 33/30 dB) of our approach under two miscalibration cases. Besides, the proposed method also shows the state-of-the-art performance under the traditional setting.

2. Related Work

Recently, plenty of advanced algorithms have been designed from diverse perspectives to reconstruct the HSI data from measurements encoded by CASSI system. Among them, optimization-based methods solve the problem by introducing diverse priors, *e.g.*, GPSR [5], TwIST [1] and GAP-TV [41] etc., in which DeSCI [22] leads to the best results. Another novel stream is to empower optimization-based method by deep learning. For example, deep unfolding methods [11, 26, 37] and Plug-and-Play (PnP) structures [30, 32, 33, 43] have been raised. Although their well interpretability and robustness to masks to a certain degree, they suffer from low efficiency and unstable convergence.

Besides, a number of deep reconstruction networks [13, 28, 29, 31, 36] have been proposed, out-standing by yielding SOTA performance with high reconstructive efficiency.

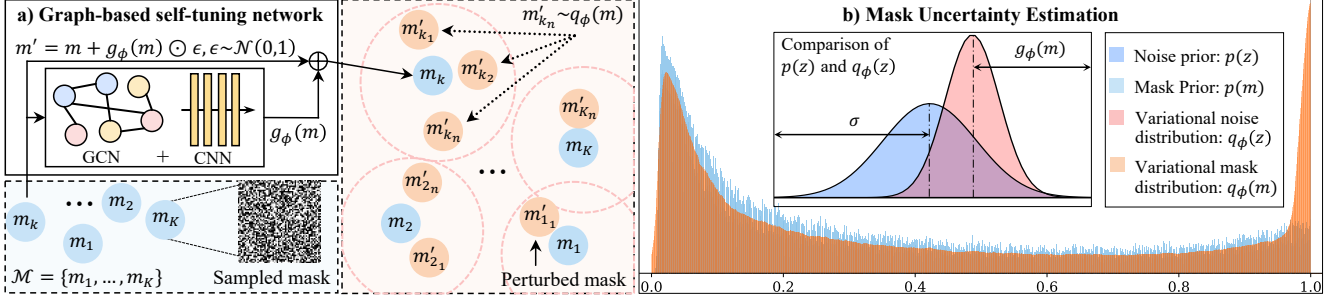


Figure 3. Illustration of Graph-based Self-Tuning (GST) network and mask uncertainty estimation. a) The Graph-based Self-Tuning network is composed of GCN and CNN. It randomly samples real mask m_k from dataset \mathcal{M} as input and produces perturbed mask $m'_{k_n} \sim q_\phi(m)$ by controlling self-tuning variance centering on m_k . b) Mask uncertainty estimation leads to a smoothed variational distribution $q_\phi(m)$ compared with the prior $p(m)$. Notably, the prior $p(m)$ is the statistical result of real masks and the variational mask distribution $q_\phi(m)$ is supported by experimental results. They are demonstrated with the same bin number. One of our observations is that the learned variational noise distribution $q_\phi(z)$ shows a smaller variance than the prior $p(z)$. We discuss this point in detail in Section 4.2.

Specifically, λ -net [31] is introduced under a generative adversarial framework. TSA-Net [28] reconstructs the HSI by jointly considering spatial/spectral self-attentions, outperforming counterparts of the day. SSI-Res-Unet (dubbed “SRN”) [36] that simply employs residual learning currently achieves leading performance among all. Recently, a GSM (Gaussian Scale Mixture)-based method [13] is proposed, showing robustness on masks by enabling an approximation on different sensing matrices. However, above pre-trained networks fail to work satisfactorily on distinct unseen masks, raising a question that how to explicitly calibrate single reconstruction network to numerous masks.

In this work, we enable adaptation to distinct real masks by proposing a variational approach to estimate mask uncertainty. Popular uncertainty estimation methods include deep ensemble [6, 19, 21], *i.e.*, training a group of networks from random weight initialization, which brings promising performance and high-quality uncertainty quantification. Bayesian neural networks (BNN) [2] forms another popular stream. They approximate variational distribution of weights by flexibly positing variational posteriors and priors. However, it’s difficult to specifically quantify mask uncertainty via a pure BNN. Also, treating masks as model weights contraries to their hardware properties.

3. Methodology

3.1. Preliminaries

HSI reconstruction. The reconstruction based on spectral CASSI system [28, 42] generally includes a hardware-encoding forward process and a software-decoding inverse process. Let x be a 3D hyperspectral image with the size of $H \times W \times \Lambda$, where H , W , and Λ represent the height, width, and the number of total spectral channels. The optical hardware encoder will compress the datacube x into a 2D measurement y upon a fixed physical mask m . The

forward model of CASSI is given by

$$y = F(x; m) = \sum_{\lambda}^{\Lambda} \text{shift}(x)_{\lambda} \odot \text{shift}(m)_{\lambda} + \zeta, \quad (1)$$

where λ refers to a spectral channel, \odot represents the element-wise product, and ζ denotes the measurement noise. The shift operation is implemented by a single disperser as $\text{shift}(x)(u, v, i) = x(h, w + d(i - \lambda), i)$. In essence, the measurement y is captured by spectral modulation¹ conditioning on the hardware mask m .

In the inverse process, we adopt a deep reconstruction network as the decoder: $\hat{x} = f_{\theta}(m, y)$ where \hat{x} is the retrieved hyperspectral image, and θ represents all the learnable parameters in the network. Let $\mathcal{D} = \{(x_i, y_i)\}_{i=1}^N$ be the dataset. The reconstruction network f_{θ} is generally trained to minimize an ℓ_1 or ℓ_2 loss as the following:

$$\min_{\theta} \sum_{x, y \in \mathcal{D}} \ell(f_{\theta}(m, y) - x) \text{ where } y = F(x; m). \quad (2)$$

We instantiate f_{θ} as a recent HSI backbone model provided in [36], which benefits from nested residual learning and spatial/spectral-invariant learning. We employ this backbone for its lightweight structure to simplify the training.

Hardware miscalibration. As shown in (2), there is a *paired relationship* between the parameter θ and mask m in deep HSI models. Thus, for different CASSI systems (*i.e.*, distinct masks), multiple pairs $\{m_1; \theta_1\}, \dots, \{m_K; \theta_K\}$ are expected for previous works. Empirically, the miscalibration between m and θ will lead to obvious performance degradation. This miscalibration issue inevitably impairs the flexibility and robustness of deploying deep HSI models across real systems, considering the expensive training time and various noises existing in hardware. To alleviate such a problem, one straight-forward solution is to train the model f_{θ} with multiple masks, *i.e.*, $\mathcal{M} = \{m_1, \dots, m_K\}$, falling in a similar strategy to deep ensemble [19]. However, directly training a single network with random masks cannot

¹We used a two-pixel shift for neighbored spectral channels following [28, 36]. More details about spectral modulation could be found in [42].

provide satisfactory performance to unseen masks (see Section 4), since the lack of explicitly exploring the relationship between uncertainties and different mask structures.

3.2. Mask Uncertainty

Modeling mask uncertainty is challenging due to 1) the high dimensionality of a 2D mask and the limited mask set size (*i.e.*, K for \mathcal{M}) and 2) the varying spatial structures among masks. Hence, we propose to first estimate uncertainties around each mask through one possible mask decomposition in this section and then reason how the uncertainty will adapt to the change of mask structures with a self-tuning network in Section 3.3.

Inspired by the distribution of real mask values (Fig. 3), which renders two peaks at 0 and 1 and appears a Gaussian shape spreading over the middle, we decompose a mask as

$$m = \tilde{m} + z, \quad (3)$$

where we assume each pixel in z follows a Gaussian distribution. For simplicity, we slightly abuse the notations by denoting the noise prior as $p(z) = \mathcal{N}(\mu, \sigma)$. The \tilde{m} denotes the underlying clean mask, which should be a binary map with diverse spatial patterns.

We estimate the mask uncertainty by approximating the mask posterior $p(m|X, Y)$ following [2, 7, 40], where $X = \{x_1, \dots, x_N\}$ and $Y = \{y_1, \dots, y_N\}$ indicate hyperspectral images and their corresponding measurements. To this end, we aim to learn a variational distribution $q_\phi(m)$ parameterized by ϕ to minimize the KL-divergence between $q_\phi(m)$ and $p(m|X, Y)$, *i.e.*, $\min_\phi KL[q_\phi(m)||p(m|X, Y)]$, equivalent to maximizing the evidence lower bound (ELBO) [12, 17] as

$$\max_\phi \underbrace{\mathbb{E}_{q_\phi(m)}[\log p(X|Y, m)]}_{\text{reconstruction}} - \underbrace{KL[q_\phi(m)||p(m)]}_{\text{regularization}}, \quad (4)$$

where the first term measures the reconstruction (*i.e.*, reconstructing the observations X based on the measurements Y and mask m via $f_\theta(m, y)$) and the second term regularizes $q_\phi(m)$ given the mask prior $p(m)$.

Inspired by Eq. (3), we treat the clean mask \tilde{m} as a 2D constant with a particular spatial pattern and focus on mask uncertainties arising from the noise z . Thus, the variational distribution $q_\phi(m)$ is defined as a Gaussian distribution centering on a given $m \in \mathcal{M}$ by

$$q_\phi(m) = \mathcal{N}(m, g_\phi(m)), \quad (5)$$

where $g_\phi(m)$ learns *self-tuning variance* to model the uncertainty adapting to real masks sampled from \mathcal{M} . Correspondingly, the underlying variational noise distribution $q_\phi(z)$ follows Gaussian distribution with variance $g_\phi(m)$. We adopt the reparameterization trick [17] for computing stochastic gradients for the expectation w.r.t $q_\phi(m)$. Specifically, let $m' \sim q_\phi(m)$ be a random variable sampled from the variational distribution, we have

$$m' = t(\phi, \epsilon) = m + g_\phi(m) \odot \epsilon, \quad \epsilon \sim \mathcal{N}(0, 1). \quad (6)$$

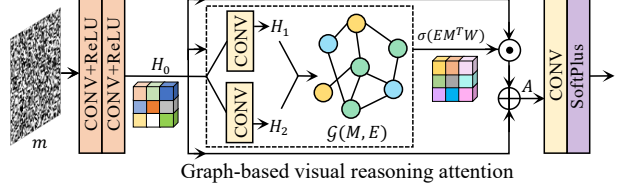


Figure 4. Structure of Graph-based Self-Tuning (GST) network. The model takes mask m as input and generates a 2D variance map. The mask is globally handled in the graph domain.

Notably, we clamp all the pixel values of m' in range $[0, 1]$.

Similar to AutoEncoders, the first term in Eq. (4) reconstructs x with the probability $p(x|y, m) \propto p(x|\hat{x}) = f_\theta(m, y)$, yielding a squared error when $x|\hat{x}$ follows a Gaussian distribution [35]. Thus, we implement the negative log-likelihood $\mathbb{E}_{q_\phi(m)}[-\log p(X|Y, m)]$ as a ℓ_2 loss and compute its Monte Carlo estimates with Eq. (6) as

$$\ell(\phi, \theta; \mathcal{D}) = \frac{N}{B} \sum_{i=1}^B \|f_\theta(y_i, t(\phi, \epsilon_i)) - x_i\|^2, \quad (7)$$

where $(x_i, y_i) \in \mathcal{D}$, B denotes the mini-batch size, and $t(\phi, \epsilon_i)$ represents the i -th sample from $q_\phi(m)$. We leverage $t(\phi, \epsilon_i)$ to sample B perturbed masks from $q_\phi(m)$ centering on one randomly sampled mask $m \in \mathcal{M}$ per batch.

Since $p(m)$ is unknown due to various spatial structures of masks, we resort to approximating the KL term in (4) with the entropy of $q_\phi(m)$. Eventually, we implement the ELBO($q(m)$) with the following loss:

$$\mathcal{L}(\phi, \theta; \mathcal{D}) = \ell(\phi, \theta; \mathcal{D}) + \beta \mathbb{H}[\log q_\phi(m)], \quad (8)$$

where $\mathbb{H}[\log q_\phi(m)]$ is computed by $\ln(g_\phi(m)\sqrt{2\pi e})$ and $\beta > 0$ interprets the objective function between variational inference and variational optimization [15, 27].

3.3. Graph-based Self-Tuning Network

We propose a graph-based self-tuning (GST) network to instantiate the variance model $g_\phi(m)$ in Eq. (5), which captures uncertainties around each mask and leads to a smoother mask distribution over real masks (see Fig. 3). The key of handling unseen masks (new hardware) is to learn how the distribution will change along with the varying spatial structures of masks. To this end, we implement the GST as a visual reasoning attention network [4, 20, 46]. It firstly computes pixel-wise correlations (visual reasoning) based on neural embeddings and then generates attention scores based on graph convolutional networks (GCN) [18, 34]. Unlike previous works [4, 20, 46], the proposed GST model is tailored for building a stochastic probabilistic encoder to capture the mask distribution.

We show the network structure of GST in Fig. 4. Given a real mask m , GST produces neural embedding H_0 by using two concatenated CONV-ReLU blocks. Then, we employ two convolutional layers to convert H_0 into two different embeddings H_1 and H_2 and generate a graph representation by matrix multiplication $H_1^T H_2$, resulting in $\mathcal{G}(M, E)$,

where the node matrix M represents mask pixels and the edge matrix E denotes the pixel-wise correlations. Let W be the weight matrix of GCN. We obtain an enhanced attention cube by pixel-wise multiplication

$$A = H_0 \odot (\sigma(EM^TW) + 1), \quad (9)$$

where σ is the sigmoid function. Finally, the self-tuning variance is obtained by

$$g_\phi(m) = \delta(\text{CONV}(A)), \quad (10)$$

where δ denotes the softplus function and ϕ denotes all the learnable parameters. Consequently, GST enables adaptive variance modeling to arbitrary real masks.

Algorithm 1: GST Training Algorithm

Input: $\mathcal{D}^{trn}, \mathcal{D}^{val}, \mathcal{M}$; initialized θ, ϕ ;
Output: θ^*, ϕ^*

- 1 Pre-train $f_\theta(\cdot)$ on \mathcal{D}^{trn} with α_0 for T^{init} epochs;
- 2 **while** not converge **do**
- 3 **for** $t = 1, \dots, T^{trn}$ **do**
- 4 $\{(x_i, y_i)\}_{i=1}^B \sim \mathcal{D}^{trn}$;
- 5 $\theta \leftarrow \theta - \alpha_1 \frac{\partial}{\partial \theta} \ell(\phi, \theta; \mathcal{D}^{trn})$;
- 6 **end**
- 7 **for** $t = 1, \dots, T^{val}$ **do**
- 8 $\{(x_i, y_i)\}_{i=1}^B \sim \mathcal{D}^{val}$, $m \sim \mathcal{M}$, $\epsilon \sim \mathcal{N}(0, 1)$;
- 9 $\phi \leftarrow \phi - \alpha_2 \frac{\partial}{\partial \phi} \mathcal{L}(\phi, \theta; \mathcal{D}^{val})$;
- 10 **end**
- 11 **end**

3.4. Bilevel Optimization

While it is possible to jointly train the HSI reconstruction network f_θ and the self-tuning network g_ϕ using the loss in Eq. 8, it is more proper to formulate the training of these two networks as a bilevel optimization framework accounting for two hyperparameter properties of masks. First, the deep reconstruction network is generally high-sensitive to the change/perturbation of masks. Thus, the model weight θ is largely subject to a mask m . Second, deep HSI methods [28, 36] usually employ a single mask and a group of shifting operations to lift the 2D measurement as a multi-channel input, where the mask works as a hyperparameter of data augmentation for training deep networks.

To be specific, we define the lower-level problem as HSI reconstruction and the upper-level problem as mask uncertainty estimation, and propose the final objective function of our GST model as the following:

$$\min_{\phi} \mathcal{L}(\phi, \theta^*; \mathcal{D}^{val}) \text{ s.t. } \theta^* = \operatorname{argmin}_{\theta} \ell(\phi, \theta; \mathcal{D}^{trn}), \quad (11)$$

where $\ell(\phi, \theta; \mathcal{D}^{trn})$ is provided in Eq. (7) with a training set and $\mathcal{L}(\phi, \theta^*; \mathcal{D}^{val})$ is given by applying Eq. (8) in a validation set. Upon Eq. (11), f_θ and g_ϕ are alternatively updated by computing gradients $\frac{\partial \ell}{\partial \theta}$ and $\frac{\partial \mathcal{L}}{\partial \phi}$. To obtain a good initialization of parameter θ , we pre-train the reconstruction network $f_\theta(m, y)$ for several epochs. The entire training

process of the proposed GST is summarized in Algorithm 1.

The benefits of introducing Eq. (11) lies in two aspects. 1) It could balance the solutions of HSI reconstruction and mask uncertainty estimation. 2) It enables the proposed GST as a hyperparameter optimization method, which could provide high-fidelity reconstruction performance even working on a single mask (see Table 3).

4. Experiments

Simulation data. We adapt the training set provided in [28]. Simulated measurements are computed by mimicking the compressing process of SD-CASSI optical system [28]. For both metric and perceptual comparison, we employ a benchmark test set that contains ten $256 \times 256 \times 28$ HSIs following [13, 30, 36]. We build a validation set by splitting 40 HSIs from the training set.

Real data. We use five real measurements provided in [28] for qualitative evaluation. We still train the model on simulation data due to the inaccessibility of real-world HSI reference. Also, the Gaussian noise ($\mathcal{N}(0, \varphi)$, $\varphi \sim U[0, 0.05]$) is added on the simulated measurements during training, for the sake of mimicking practical measurement noise ζ . To sum up, all settings are kept the same as compared deep reconstructive methods.

Mask set. We adopt two 660×660 hardware masks in our experiment. Both are produced by the same fabrication process. For training, the mask set \mathcal{M} is created by randomly cropping (256×256) from the mask provided in [28]. For testing, both masks are applied. In simulation, testing masks are differentiated from the training ones. For real HSI reconstruction, the second mask [29] is applied, indicating hardware miscalibration scenario.

Implementation details. The training procedures (Algorithm. 1) for simulation and real case follow the same schedule: We apply the `xavier uniform` [9] initializer with `gain=1`. Before alternating, the reconstruction network is trained for $T^{init}=20$ epochs (learning rate $\alpha_0=4 \times 10^{-4}$). Then, the reconstruction network $f_\theta(\cdot)$ is updated on training phase for $T^{trn}=5$ epochs ($\alpha_1=4 \times 10^{-4}$) and the GST network is updated on validation phase for $T^{val}=3$ epochs ($\alpha_2=1 \times 10^{-5}$). The learning rates are halved per 50 epochs and we adopt Adam optimizer [16] with default setting. In this work, we choose the best-performed version (v1) of (SRN) [36] as the reconstructive backbone, *i.e.*, the full network without rescaling pairs. Implementation is conducted on 4 NVIDIA GeForce GTX 3090 GPUs.

Compared methods. For hardware miscalibration, masks for data pair setup (*i.e.*, CASSI compressing procedure) and network training should be different from those for testing. We specifically consider two scenarios: 1) many-to-many, *i.e.*, training the model on mask set \mathcal{M} and testing it by unseen masks; 2) One-to-many, *i.e.*, training the model on single mask and testing it by diverse un-

Table 1. PSNR(dB)/SSIM by different methods on 10 simulation scene under hardware miscalibration (many-to-many): method is trained on mask set \mathcal{M} and tested by unseen random masks. Note that † indicates that PnP-DIP is a mask-free method, which reconstructs from measurements encoded by random masks. For all methods, the *mean* and *std* are obtained upon 100 testing trials.

| Scene | TSA-Net [28] | | GSM [13] | | PnP-DIP † [30] | | SRN [36] | | Ours | |
|-------|------------------|---------------------|------------------|---------------------|-------------------------|---------------------|------------------|---------------------|----------------------------------|-------------------------------------|
| | PSNR | SSIM | PSNR | SSIM | PSNR | SSIM | PSNR | SSIM | PSNR | SSIM |
| 1 | 23.45 \pm 0.29 | 0.6569 \pm 0.0051 | 31.38 \pm 0.20 | 0.8826 \pm 0.0032 | 29.24 \pm 0.98 | 0.7964 \pm 0.0532 | 33.26 \pm 0.16 | 0.9104 \pm 0.0018 | 33.99\pm0.14 | 0.9258\pm0.0013 |
| 2 | 18.52 \pm 0.12 | 0.5511 \pm 0.0049 | 25.94 \pm 0.22 | 0.8570 \pm 0.0041 | 25.73 \pm 0.54 | 0.7558 \pm 0.0117 | 29.86 \pm 0.23 | 0.8809 \pm 0.0029 | 30.49\pm0.17 | 0.9002\pm0.0022 |
| 3 | 18.42 \pm 0.30 | 0.5929 \pm 0.0127 | 26.11 \pm 0.20 | 0.8874 \pm 0.0034 | 29.61 \pm 0.45 | 0.8541 \pm 0.0125 | 31.69 \pm 0.20 | 0.9093 \pm 0.0020 | 32.63\pm0.16 | 0.9212\pm0.0013 |
| 4 | 30.44 \pm 0.15 | 0.8940 \pm 0.0043 | 34.72 \pm 0.35 | 0.9473 \pm 0.0023 | 38.21 \pm 0.66 | 0.9280 \pm 0.0078 | 39.90 \pm 0.22 | 0.9469 \pm 0.0012 | 41.04\pm0.23 | 0.9667\pm0.0014 |
| 5 | 20.89 \pm 0.23 | 0.5648 \pm 0.0077 | 26.15 \pm 0.24 | 0.8256 \pm 0.0061 | 28.59 \pm 0.79 | 0.8481 \pm 0.0183 | 30.86 \pm 0.16 | 0.9232 \pm 0.0019 | 31.49\pm0.17 | 0.9379\pm0.0017 |
| 6 | 23.04 \pm 0.19 | 0.6099 \pm 0.0060 | 30.97 \pm 0.29 | 0.9224 \pm 0.0025 | 29.70 \pm 0.51 | 0.8484 \pm 0.0186 | 34.20 \pm 0.23 | 0.9405 \pm 0.0014 | 34.89\pm0.29 | 0.9545\pm0.0009 |
| 7 | 15.97 \pm 0.14 | 0.6260 \pm 0.0042 | 22.58 \pm 0.24 | 0.8459 \pm 0.0054 | 27.13 \pm 0.31 | 0.8666 \pm 0.0079 | 27.27 \pm 0.16 | 0.8515 \pm 0.0026 | 27.63\pm0.16 | 0.8658\pm0.0024 |
| 8 | 22.64 \pm 0.18 | 0.6366 \pm 0.0066 | 29.76 \pm 0.22 | 0.9059 \pm 0.0021 | 28.38 \pm 0.35 | 0.8325 \pm 0.0203 | 32.35 \pm 0.22 | 0.9320 \pm 0.0015 | 33.02\pm0.26 | 0.9471\pm0.0013 |
| 9 | 18.91 \pm 0.11 | 0.5946 \pm 0.0083 | 27.23 \pm 0.11 | 0.8899 \pm 0.0021 | 33.63 \pm 0.26 | 0.8779 \pm 0.0073 | 32.83 \pm 0.13 | 0.9205 \pm 0.0016 | 33.45\pm0.13 | 0.9317\pm0.0013 |
| 10 | 21.90 \pm 0.18 | 0.5249 \pm 0.0110 | 28.05 \pm 0.21 | 0.8877 \pm 0.0055 | 27.24 \pm 0.43 | 0.7957 \pm 0.0226 | 30.25 \pm 0.14 | 0.9053 \pm 0.0019 | 31.49\pm0.15 | 0.9345\pm0.0015 |
| Avg. | 21.42 \pm 0.07 | 0.6162 \pm 0.0030 | 28.20 \pm 0.01 | 0.8852 \pm 0.0001 | 29.66 \pm 0.38 | 0.8375 \pm 0.0093 | 32.24 \pm 0.10 | 0.9121 \pm 0.0010 | 33.02\pm0.01 | 0.9285\pm0.0001 |

Table 2. PSNR(dB)/SSIM by different methods on 10 simulation scenes under hardware miscalibration (one-to-many): method is trained by single mask and tested by random masks. Note that † indicates that PnP-DIP is a mask-free method, which reconstructs from measurements encoded by random masks. The *mean* and *std* are obtained upon 100 testing trials.

| Scene | TSA-Net [28] | | GSM [13] | | PnP-DIP † [30] | | SRN [36] | | Ours | |
|-------|------------------|---------------------|------------------|---------------------|-------------------------|---------------------|------------------|---------------------|----------------------------------|-------------------------------------|
| | PSNR | SSIM | PSNR | SSIM | PSNR | SSIM | PSNR | SSIM | PSNR | SSIM |
| 1 | 28.49 \pm 0.58 | 0.8520 \pm 0.0081 | 28.20 \pm 0.95 | 0.8553 \pm 0.0185 | 29.24 \pm 0.98 | 0.7964 \pm 0.0532 | 31.24 \pm 0.77 | 0.8878 \pm 0.0117 | 31.72\pm0.76 | 0.8939\pm0.0119 |
| 2 | 24.96 \pm 0.51 | 0.8332 \pm 0.0064 | 24.46 \pm 0.96 | 0.8330 \pm 0.0189 | 25.73 \pm 0.54 | 0.7558 \pm 0.0117 | 27.87 \pm 0.82 | 0.8535 \pm 0.0131 | 28.77\pm0.85 | 0.8552\pm0.0144 |
| 3 | 26.14 \pm 0.76 | 0.8829 \pm 0.0108 | 23.71 \pm 1.18 | 0.8077 \pm 0.0221 | 29.61 \pm 0.45 | 0.8541 \pm 0.0125 | 28.31 \pm 0.88 | 0.8415 \pm 0.0213 | 28.77\pm1.13 | 0.8405\pm0.0257 |
| 4 | 35.67 \pm 0.47 | 0.9427 \pm 0.0028 | 31.55 \pm 0.75 | 0.9385 \pm 0.0074 | 38.21 \pm 0.66 | 0.9280 \pm 0.0078 | 37.93 \pm 0.72 | 0.9476 \pm 0.0057 | 37.60\pm0.81 | 0.9447\pm0.0071 |
| 5 | 25.40 \pm 0.59 | 0.8280 \pm 0.0108 | 24.44 \pm 0.96 | 0.7744 \pm 0.0291 | 28.59 \pm 0.79 | 0.8481 \pm 0.0183 | 27.99 \pm 0.79 | 0.8680 \pm 0.0194 | 28.58\pm0.79 | 0.8746\pm0.0208 |
| 6 | 29.32 \pm 0.60 | 0.8796 \pm 0.0047 | 28.28 \pm 0.92 | 0.9026 \pm 0.0094 | 29.70 \pm 0.51 | 0.8484 \pm 0.0186 | 32.13 \pm 0.87 | 0.9344 \pm 0.0061 | 32.72\pm0.79 | 0.9339\pm0.0061 |
| 7 | 22.80 \pm 0.65 | 0.8461 \pm 0.0101 | 21.45 \pm 0.79 | 0.8147 \pm 0.0162 | 27.13 \pm 0.31 | 0.8666 \pm 0.0079 | 24.84 \pm 0.73 | 0.7973 \pm 0.0150 | 25.15\pm0.76 | 0.7935\pm0.0173 |
| 8 | 28.09 \pm 0.43 | 0.8738 \pm 0.0043 | 28.08 \pm 0.76 | 0.9024 \pm 0.0089 | 28.38 \pm 0.35 | 0.8325 \pm 0.0203 | 31.32 \pm 0.59 | 0.9324 \pm 0.0043 | 31.84\pm0.56 | 0.9323\pm0.0042 |
| 9 | 27.75 \pm 0.55 | 0.8865 \pm 0.0054 | 26.80 \pm 0.78 | 0.8773 \pm 0.0144 | 33.63 \pm 0.26 | 0.8779 \pm 0.0073 | 31.06 \pm 0.66 | 0.8997 \pm 0.0091 | 31.11\pm0.72 | 0.8988\pm0.0104 |
| 10 | 26.05 \pm 0.48 | 0.8114 \pm 0.0072 | 26.40 \pm 0.77 | 0.8771 \pm 0.0124 | 27.24 \pm 0.43 | 0.7957 \pm 0.0226 | 29.01 \pm 0.61 | 0.9028 \pm 0.0092 | 29.50\pm0.68 | 0.9030\pm0.0098 |
| Avg. | 27.47 \pm 0.46 | 0.8636 \pm 0.0060 | 26.34 \pm 0.06 | 0.8582 \pm 0.0012 | 29.66 \pm 0.38 | 0.8375 \pm 0.0093 | 30.17 \pm 0.63 | 0.8865 \pm 0.0108 | 30.60\pm0.08 | 0.8881\pm0.0013 |

seen masks, which brings more challenges. For quantitative performance comparison, in this work all the testing results are computed upon 100 testing trials (100 random unseen masks). We compare with four SOTA methods: TSA-Net [28], GSM-based method [13], SSI-ResUNet (SRN) [36] and PnP-DIP [30], among which the first three are deep reconstruction networks. Note that 1) PnP-DIP is a self-supervised method. We test it by feeding the data encoded by different masks in the testing mask set and compute the performance over all obtained results. 2) For real-world HSI reconstruction, all models are trained on the same mask while tested on the other. Specifically, the network inputs are initialized by testing mask for TSA-Net and SRN. For GSM, as demonstrated by the authors, we directly compute the sensing matrix of testing mask and replace the corresponding approximation in the network. We use PSNR and SSIM [39] as metrics for quantitative comparison.

4.1. HSI Reconstruction Performance

We evaluate our method under different settings and provide results on both simulation and real data. More visualizations are provided in the supplementary material.

Miscalibration (many-to-many). As discussed at the end of Section 3.1, training the deep reconstruction models on a mask set serves as a potential solution. Besides, this

leads to a fair comparison between our proposed method and others. In Table 1, we report the mean values and standard deviation values of different methods in terms of PSNR and SSIM. Our method outperforms others by reconstructing high-fidelity HSI, *i.e.*, the only method achieves over 33dB regarding averaged PSNR. In Fig. 5, the reconstructive results are perceptually compared. Our method retrieves more details at different spectral channels. We randomly choose two regions, corresponding to two colors separately (patch a and b in RGB reference), to analyze results regarding spectra. Density curves along with correlations to ground truth are compared as in Fig. 5 (bottom-left).

Miscalibration (one-to-many). In this setting, method is trained on a single mask and tested on multiple masks. Such a setting actually is unfair to ours – it’s hard for the proposed method to learn a complete variational distribution given one real mask. As compared in the Table 2, except for the mask-free method, PnP-DIP, all the other methods experience large performance degradation. Even so, our method demonstrates more robustness than the others, outperforming SRN by 0.43dB/0.0016 (PSNR/SSIM).

Same mask (one-to-one). Although the proposed method requires multiple masks for the distribution modeling, leveraging the same real mask for CASSI optical system and reconstruction is still a common practice. For this

Table 3. PSNR (dB) and SSIM values by different algorithms on the simulation dataset under the **same mask** reconstruction setting. Note that our method is trained on the same 256×256 real mask for a fair comparison.

| Methods | Scene1 | | Scene2 | | Scene3 | | Scene4 | | Scene5 | | Scene6 | | Scene7 | | Scene8 | | Scene9 | | Scene10 | | Avg. | |
|----------------|--------------|---------------|--------------|---------------|--------------|---------------|--------------|---------------|--------------|---------------|--------------|---------------|--------------|---------------|--------------|---------------|--------------|---------------|--------------|---------------|--------------|---------------|
| | PSNR | SSIM |
| λ -net | 30.82 | 0.8492 | 26.30 | 0.8054 | 29.42 | 0.8696 | 37.37 | 0.9338 | 27.84 | 0.8166 | 30.69 | 0.8527 | 24.20 | 0.8062 | 28.86 | 0.8307 | 29.32 | 0.8258 | 27.66 | 0.8163 | 29.25 | 0.8406 |
| HSSP | 31.07 | 0.8577 | 26.30 | 0.8422 | 29.00 | 0.8231 | 38.24 | 0.9018 | 27.98 | 0.8084 | 29.16 | 0.8766 | 24.11 | 0.8236 | 27.94 | 0.8811 | 29.14 | 0.8676 | 26.44 | 0.8416 | 28.93 | 0.8524 |
| TSA-Net | 31.26 | 0.8920 | 26.88 | 0.8583 | 30.03 | 0.9145 | 39.90 | 0.9528 | 28.89 | 0.8835 | 31.30 | 0.9076 | 25.16 | 0.8782 | 29.69 | 0.8884 | 30.03 | 0.8901 | 28.32 | 0.8740 | 30.24 | 0.8939 |
| GSM | 32.38 | 0.9152 | 27.56 | 0.8977 | 29.02 | 0.9251 | 36.37 | 0.9636 | 28.56 | 0.8820 | 32.49 | 0.9372 | 25.19 | 0.8860 | 31.06 | 0.9234 | 29.40 | 0.9110 | 30.74 | 0.9247 | 30.28 | 0.9166 |
| PnP-DIP | 31.99 | 0.8633 | 26.56 | 0.7603 | 30.06 | 0.8596 | 38.99 | 0.9303 | 29.09 | 0.8490 | 29.68 | 0.8481 | 27.68 | 0.8639 | 29.01 | 0.8412 | 33.35 | 0.8802 | 27.98 | 0.8327 | 30.44 | 0.8529 |
| SRN | 34.13 | 0.9260 | 30.60 | 0.8985 | 32.87 | 0.9221 | 41.27 | 0.9687 | 31.66 | 0.9376 | 35.14 | 0.9561 | 27.93 | 0.8638 | 33.14 | 0.9488 | 33.49 | 0.9326 | 31.43 | 0.9338 | 33.17 | 0.9288 |
| Ours | 34.19 | 0.9292 | 31.04 | 0.9014 | 32.93 | 0.9224 | 40.71 | 0.9672 | 31.83 | 0.9415 | 35.14 | 0.9543 | 28.08 | 0.8628 | 33.18 | 0.9486 | 33.50 | 0.9332 | 31.59 | 0.9311 | 33.22 | 0.9292 |

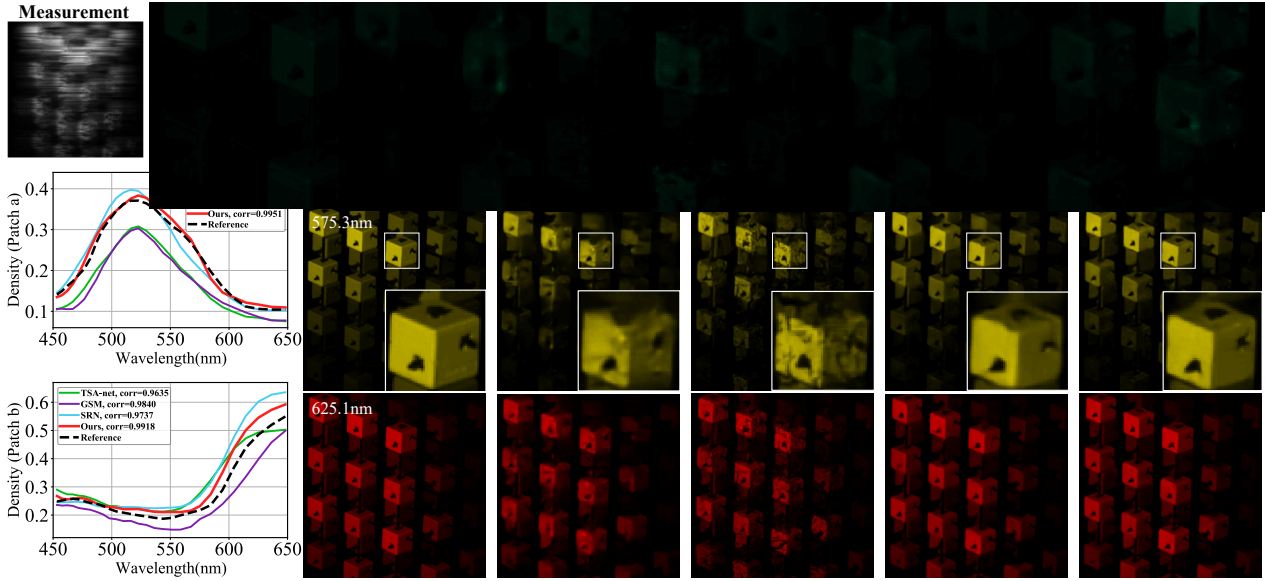


Figure 5. Reconstruction results on one simulation scene under hardware miscalibration (many-to-many). All methods are trained on the mask set \mathcal{M} and tested by one unseen mask. Density curves computed on chosen patches are compared to analysis the spectra.

reason, we apply the proposed method into this traditional setting, which is training and testing the model on a single mask. As shown in Table 3, our method still demonstrates a promising reconstructive performance. The underlying intuition is that compared to the reconstructive backbone, our model is more powerful by employing more parameters.

Results on real data. Fig. 6 visualizes reconstruction results on the real dataset following [28], where the *left* provides results using the same mask and the *right* is under the one-to-many miscalibration setting. For the same mask, the proposed method performs comparably. For the miscalibration, we train all the models on a single real mask provided in [28] and test them on the mask given in [29]. As can be seen, the proposed method produces plausible results and improves over other methods visually.

4.2. Model Discussion

Ablation study. In Table 4 we compare the performance of our proposed method with three ablated models: w/o GST Net, w/o bilevel optimization, w/o GCN in Self-Tuning Net. 1) The setting of w/o GST Net actually degrades into the reconstructive back-

Table 4. Ablation study of the proposed method under the setting of miscalibration (many-to-many) among 100 testing trials.

| Settings | PSNR(dB) | SSIM |
|----------------------------|------------------|---------------------|
| w/o GST Net | 32.24 ± 0.10 | 0.9121 ± 0.0010 |
| w/o bilevel optimization | 32.43 ± 0.02 | 0.9206 ± 0.0001 |
| w/o GCN in Self-Tuning Net | 32.82 ± 0.01 | 0.9262 ± 0.0001 |
| Our full model | 33.02 ± 0.01 | 0.9285 ± 0.0001 |

bone SRN under miscalibration (many-to-many). 2) The setting w/o bilevel optimization is implemented by training all learnable parameters in a single-level. 3) For w/o GCN in Self-Tuning Net, we exchange the GCN with a convolutional layer carrying more parameters. We uncover the superiority of the graph-based self-tuning network and find that random-mask training only leads to sub-optimal performance. Also, the effectiveness of proposed learning fashions, *i.e.*, bilevel optimization together with graph-based learning are also demonstrated.

Self-tuning variance under different priors. As shown by the green curve in Fig. 7 (a), we explored different values ranging from 0 to 1 as fixed variance and check the poten-

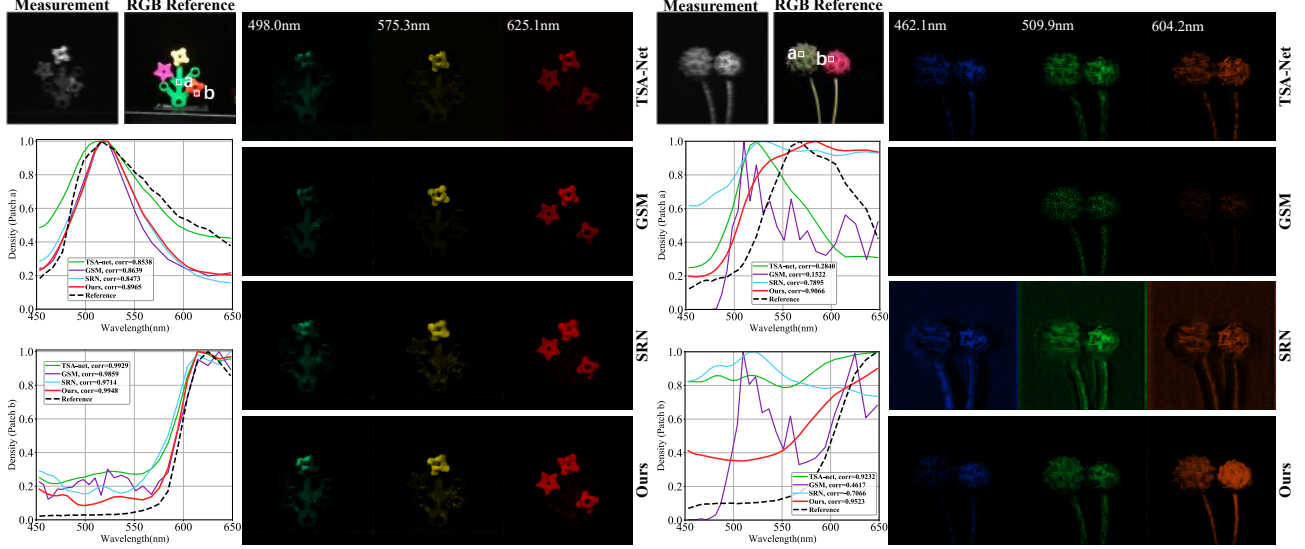


Figure 6. Real HSI reconstruction. **Left:** same mask (one-to-one) reconstruction, *i.e.*, all methods are trained and tested on the same 660×660 real mask. **Right:** miscalibration (one-to-many) setting, *i.e.*, all methods are trained on a single mask and tested by unseen masks (Here we adopt another 660×660 real mask). Density curves computed on chosen patches are compared to analysis the spectra.

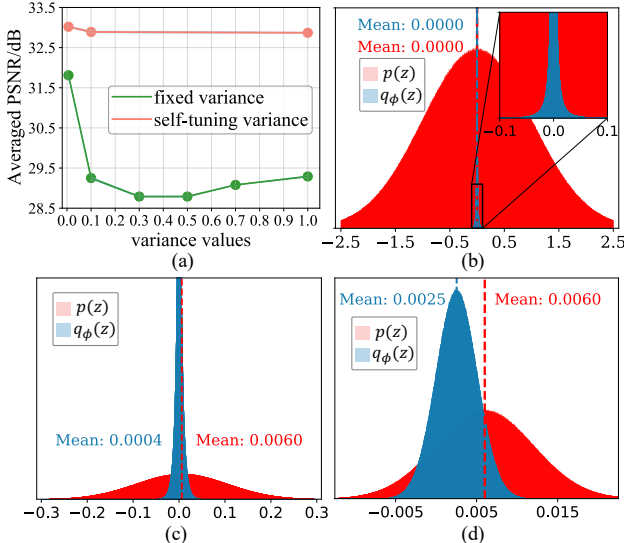


Figure 7. Discussion on self-tuning variance. (a) Performance comparison between self-tuning variance and fixed ones. (b) The standard normal prior $\mathcal{N}(0, 1)$. (c) Set the prior as $\mathcal{N}(0.006, 0.1)$ by observing real masks. (d) Set the prior as $\mathcal{N}(0.006, 0.005)$ by observing real masks and the performance curve in (a).

tial capabilities. A performance improvement can be observed when the variance is sufficiently small. The value of 0.005 gives best performance, indicating a relatively strong prior. Bearing these observations, we explore the behavior of self-tuning variance under different noise priors. Specifically, we implement the noise prior $p(z)$ by exchanging the standard normal distribution of auxiliary variable ϵ in Eq. (6). Given different priors, variational noise distribution with reduced intensity is expected. We start from $\mathcal{N}(0, 1)$,

which is so broad that the GST network tries to centralize variational noise and restricting the randomness as Fig. 7 (b) shown. Therefore, we take a more specific prior with smaller variance, *i.e.*, $\mathcal{N}(0.006, 0.1)$. By adopting minimum value of real mask as the noise mean, we focus on the noise concentrates around zero. The corresponding variational noise distribution deviates from the prior as shown in Fig. 7 (c), indicating the underlying impact of GST network. Finally, as the minimum value previously posited performs best among all fixed values, we employ it into $p(z)$, yielding $\mathcal{N}(0.006, 0.005)$. As the red curve in Fig. 7 (a) indicated, the best reconstruction performance is also obtained. In summary, the proposed method effectively restricts the posited noise prior, leading to the variational noise distribution with a reduced range. The learned self-tuning variance yields superior performance than the fixed variance values. Besides, the self-tuning variance brings about a stable reconstruction performance under different noise priors.

5. Conclusions

In this work, we have explored a practical hardware miscalibration issue when deploying deep HSI models in real CASSI systems. Our solution is to calibrate a single reconstruction network via modeling mask uncertainty. We proposed a complete variational Bayesian learning treatment upon one possible mask decomposition inspired by observations on real masks. Bearing the objectives of variational mask distribution modeling and HSI retrieval, we introduced and implemented a novel Graph-based Self-Tuning (GST) network that proceeds HSI reconstruction and uncertainty reasoning under a bilevel optimization framework. The proposed method enabled a smoothed distribution and

achieved promising performance under two different miscalibration scenarios. We hope the proposed insight will benefit future work in this novel research direction.

References

- [1] José M Bioucas-Dias and Mário AT Figueiredo. A new twist: Two-step iterative shrinkage/thresholding algorithms for image restoration. *TIP*, 2007. [2](#)
- [2] Charles Blundell, Julien Cornebise, Koray Kavukcuoglu, and Daan Wierstra. Weight uncertainty in neural network. In *ICML*, 2015. [3, 4](#)
- [3] Marcus Borengasser, William S Hungate, and Russell Watkins. *Hyperspectral remote sensing: principles and applications*. CRC press, 2007. [1](#)
- [4] Xinlei Chen, Li-Jia Li, Li Fei-Fei, and Abhinav Gupta. Iterative visual reasoning beyond convolutions. In *CVPR*, 2018. [4](#)
- [5] Mário AT Figueiredo, Robert D Nowak, and Stephen J Wright. Gradient projection for sparse reconstruction: Application to compressed sensing and other inverse problems. *IEEE Journal of selected topics in signal processing*, 2007. [2](#)
- [6] Stanislav Fort, Huiyi Hu, and Balaji Lakshminarayanan. Deep ensembles: A loss landscape perspective. *arXiv preprint arXiv:1912.02757*, 2019. [3](#)
- [7] Yarin Gal. *Uncertainty in Deep Learning*. PhD thesis, University of Cambridge, 2016. [4](#)
- [8] Michael E Gehm, Renu John, David J Brady, Rebecca M Willett, and Timothy J Schulz. Single-shot compressive spectral imaging with a dual-disperser architecture. *Optics express*, 2007. [1](#)
- [9] Xavier Glorot and Yoshua Bengio. Understanding the difficulty of training deep feedforward neural networks. In *AISTATS*, 2010. [5](#)
- [10] Aoife A Gowen, Colm P O'Donnell, Patrick J Cullen, Gérard Downey, and Jesus M Frias. Hyperspectral imaging—an emerging process analytical tool for food quality and safety control. *Trends in food science & technology*, 18(12):590–598, 2007. [1](#)
- [11] John R Hershey, Jonathan Le Roux, and Felix Weninger. Deep unfolding: Model-based inspiration of novel deep architectures. *arXiv preprint arXiv:1409.2574*, 2014. [2](#)
- [12] Matthew D Hoffman and Matthew J Johnson. Elbo surgery: yet another way to carve up the variational evidence lower bound. In *NeurIPS Workshop*, 2016. [4](#)
- [13] Tao Huang, Weisheng Dong, Xin Yuan, Jinjian Wu, and Guangming Shi. Deep gaussian scale mixture prior for spectral compressive imaging. In *CVPR*, 2021. [1, 3, 5, 6](#)
- [14] William R Johnson, Daniel W Wilson, Wolfgang Fink, Mark S Humayun, and Gregory H Bearman. Snapshot hyperspectral imaging in ophthalmology. *Journal of biomedical optics*, 12(1):014036, 2007. [1](#)
- [15] Mohammad Khan, Didrik Nielsen, Voot Tangkaratt, Wu Lin, Yarin Gal, and Akash Srivastava. Fast and scalable bayesian deep learning by weight-perturbation in adam. In *ICML*, 2018. [4](#)
- [16] Diederik P Kingma and Jimmy Ba. Adam: A method for stochastic optimization. *arXiv preprint arXiv:1412.6980*, 2014. [5](#)
- [17] Diederik P Kingma and Max Welling. Auto-encoding variational bayes. *arXiv preprint arXiv:1312.6114*, 2013. [4](#)
- [18] Thomas N Kipf and Max Welling. Semi-supervised classification with graph convolutional networks. In *ICLR*, 2017. [4](#)
- [19] Balaji Lakshminarayanan, Alexander Pritzel, and Charles Blundell. Simple and scalable predictive uncertainty estimation using deep ensembles. In *NeurIPS*, 2017. [2, 3](#)
- [20] Kunpeng Li, Yulun Zhang, Kai Li, Yuanyuan Li, and Yun Fu. Visual semantic reasoning for image-text matching. In *ICCV*, 2019. [4](#)
- [21] Jeremiah Zhe Liu, John Paisley, Marianthi-Anna Kioumourtzoglou, and Brent Coull. Accurate uncertainty estimation and decomposition in ensemble learning. *arXiv preprint arXiv:1911.04061*, 2019. [3](#)
- [22] Yang Liu, Xin Yuan, Jinli Suo, David J Brady, and Qionghai Dai. Rank minimization for snapshot compressive imaging. *TPAMI*, 2018. [1, 2](#)
- [23] Delia Lorente, Nuria Aleixos, JUAN Gómez-Sanchis, Sergio Cubero, OSCAR LEONARDO García-Navarrete, and José Blasco. Recent advances and applications of hyperspectral imaging for fruit and vegetable quality assessment. *Food and Bioprocess Technology*, 5(4):1121–1142, 2012. [1](#)
- [24] Guolan Lu and Baowei Fei. Medical hyperspectral imaging: a review. *Journal of biomedical optics*, 19(1):010901, 2014. [1](#)
- [25] Renfu Lu and Yud-Ren Chen. Hyperspectral imaging for safety inspection of food and agricultural products. In *Pathogen Detection and Remediation for Safe Eating*, volume 3544, pages 121–133. International Society for Optics and Photonics, 1999. [1](#)
- [26] Jiawei Ma, Xiao-Yang Liu, Zheng Shou, and Xin Yuan. Deep tensor admm-net for snapshot compressive imaging. In *ICCV*, 2019. [2](#)
- [27] Matthew MacKay, Paul Vicol, Jon Lorraine, David Duvenaud, and Roger Grosse. Self-tuning networks: Bilevel optimization of hyperparameters using structured best-response functions. *arXiv preprint arXiv:1903.03088*, 2019. [4](#)
- [28] Ziyi Meng, Jiawei Ma, and Xin Yuan. End-to-end low cost compressive spectral imaging with spatial-spectral self-attention. In *ECCV*, 2020. [1, 2, 3, 5, 6, 7](#)
- [29] Ziyi Meng, Mu Qiao, Jiawei Ma, Zhenming Yu, Kun Xu, and Xin Yuan. Snapshot multispectral endomicroscopy. *Optics Letters*, 2020. [2, 5, 7](#)
- [30] Ziyi Meng, Zhenming Yu, Kun Xu, and Xin Yuan. Self-supervised neural networks for spectral snapshot compressive imaging. In *ICCV*, 2021. [1, 2, 5, 6](#)
- [31] Xin Miao, Xin Yuan, Yunchen Pu, and Vassilis Athitsos. 1-net: Reconstruct hyperspectral images from a snapshot measurement. In *ICCV*, 2019. [2, 3](#)
- [32] Mu Qiao, Xuan Liu, and Xin Yuan. Snapshot spatial-temporal compressive imaging. *Optics letters*, 2020. [2](#)
- [33] Mu Qiao, Ziyi Meng, Jiawei Ma, and Xin Yuan. Deep learning for video compressive sensing. *APL Photonics*, 2020. [2](#)

[34] Franco Scarselli, Marco Gori, Ah Chung Tsoi, Markus Hagenbuchner, and Gabriele Monfardini. The graph neural network model. *IEEE transactions on neural networks*, 2008. [4](#)

[35] Pascal Vincent, Hugo Larochelle, Isabelle Lajoie, Yoshua Bengio, Pierre-Antoine Manzagol, and Léon Bottou. Stacked denoising autoencoders: Learning useful representations in a deep network with a local denoising criterion. *JMLR*, 2010. [4](#)

[36] Jiamian Wang, Yulun Zhang, Xin Yuan, Yun Fu, and Zhiqiang Tao. A new backbone for hyperspectral image reconstruction. *arXiv preprint arXiv:2108.07739*, 2021. [1, 2, 3, 5, 6](#)

[37] Lizhi Wang, Chen Sun, Ying Fu, Min H Kim, and Hua Huang. Hyperspectral image reconstruction using a deep spatial-spectral prior. In *CVPR*, 2019. [2](#)

[38] Lizhi Wang, Zhiwei Xiong, Guangming Shi, Feng Wu, and Wenjun Zeng. Adaptive nonlocal sparse representation for dual-camera compressive hyperspectral imaging. *TPAMI*, 2017. [1](#)

[39] Zhou Wang, Alan C Bovik, Hamid R Sheikh, and Eero P Simoncelli. Image quality assessment: from error visibility to structural similarity. *TIP*, 2004. [6](#)

[40] Andrew Gordon Wilson and Pavel Izmailov. Bayesian deep learning and a probabilistic perspective of generalization. *arXiv preprint arXiv:2002.08791*, 2020. [4](#)

[41] Xin Yuan. Generalized alternating projection based total variation minimization for compressive sensing. In *ICIP*, 2016. [2](#)

[42] Xin Yuan, David J. Brady, and Aggelos K. Katsaggelos. Snapshot compressive imaging: Theory, algorithms, and applications. *IEEE Signal Processing Magazine*, 2021. [1, 3](#)

[43] Xin Yuan, Yang Liu, Jinli Suo, and Qionghai Dai. Plug-and-play algorithms for large-scale snapshot compressive imaging. In *CVPR*, 2020. [2](#)

[44] Xin Yuan, Yang Liu, Jinli Suo, Fredo Durand, and Qionghai Dai. Plug-and-play algorithms for video snapshot compressive imaging. *TPAMI*, 2021. [1](#)

[45] Yuan Yuan, Xiangtao Zheng, and Xiaoqiang Lu. Hyperspectral image superresolution by transfer learning. *IEEE Journal of Selected Topics in Applied Earth Observations and Remote Sensing*, 10(5):1963–1974, 2017. [1](#)

[46] Yulun Zhang, Kai Li, Kunpeng Li, and Yun Fu. Mr image super-resolution with squeeze and excitation reasoning attention network. In *CVPR*, 2021. [4](#)